Local slip activities in polycrystalline α-Ti depending on textures and strain rates

Yoshiki Kawano[1)]*, Tsuyoshi Mayama[2)],

Taiki Okamoto[1)], Masatoshi Mitsuhara[3)]

1) Graduate School of Engineering, Mechanical Engineering, Kitami Institute of Technology, Kitami-shi, Hokkaido 090-8507, Japan

2) Department of Materials Science, Kumamoto University, 2-39-1 Kurokami, Chuo-ku, Kumamoto 860-8555, Japan

3) Department of Advanced Materials Science and Engineering, Faculty of Engineering Sciences, Kyushu University, Kasuga-shi, Fukuoka 816-8580, Japan

* Corresponding author: Email: kawano_y@mail.kitami-it.ac.jp

Abstract

It is possible that strain localization in polycrystalline α-Ti leads to the fracture, and it is crucial to evaluate the local slip activities for individual slip systems depending on their textures and loading conditions. In this study, the effects of textures and strain rates on local slip activities were investigated using the crystal plasticity finite element method. For the analysis, microstructural models of α-Ti with the following three textures were employed: aggregates of (0001) axes are (i) splitting in rolling direction (RD-split texture), (ii) splitting in transverse direction (TD-split texture), and (iii) aligned in normal direction (basal texture). For each texture model, two variations in the crystal orientation distributions were considered, namely, small and large scatterings of crystal orientations in the (0001) axes by normal random numbers. The differences in the strain rate sensitivities of the critical resolved shear stresses (CRSSs) among slip systems were also considered. Tensile loading was applied by a forced displacement in the RD with two strain rate conditions of 1.0×10^{-4} s^{-1} and 1.0×10^{-1} s^{-1}. Local non-prismatic slips were easier to operate in the models with basal and RD-split textures than with the TD-split texture. The slip strains for non-prismatic slip systems were higher at higher strain rates, while activities in the prismatic slips decreased with an increase in strain rates. The mechanism of the exchange of slip system activities can be explained by strain

redistribution between hard and soft regions and changes in CRSS as a function of strain rates.

KEYWORDS: crystal plasticity analysis; titanium; α-phase; strain rate; crystallographic textures; heterogeneous deformation; slip activity

1. Introduction

Titanium and its alloys with excellent mechanical properties have been used as structural materials in various fields, such as aerospace, medicine, and sports equipment [1,2]. Thus, understanding fracture mechanisms are crucial for enhancement of the safety and performance of the products. The fracture is related to the microscopic deformation mechanisms. In α titanium (α-Ti), soft grains (which easily undergo plastic deformation) and hard grains (which do not easily undergo plastic deformation) exist. Stress and strain are redistributed between the soft and hard grains during the deformation, and it is possible that the stress and strain concentration induced by the inhomogeneous deformation lead to the fracture [3–5].

The ease of plastic deformation in each grain is strongly affected by critical resolved shear stress (CRSS) as well as crystallographic orientations. Slip systems in α-Ti with hcp structure are basal slip systems (Bsl < a >), prismatic <a> slip systems (Pri < a >), 1st order pyramidal <a> slip systems (Pyr < a >), 1st order pyramidal < c + a > (Pyr-1 < c + a >), and 2nd order pyramidal <c+a>. The CRSSs are different among slip systems, and the difference strongly affect the deformation mechanism. In recent years, crystal plasticity analysis, which accurately represent deformation in crystal grain level as well as macroscopic stress-strain relationships, is typically employed to investigate the

deformation mechanisms [6–14]. The relationship between inhomogeneous deformation and CRSS ratio has been investigated by crystal plasticity analysis. Baudoin et al. (2019) represented deformation of commercially pure titanium (CP-Ti) by the crystal plasticity analysis, and reported that the heterogeneous strain distribution is attributed to the CRSS ratio [14]. Kawano et al. investigated strain distributions in polycrystalline α-Ti using crystal plasticity analysis and revealed that strain concentration can appear because of strain redistribution between soft and hard regions [13,15]; an imbalance in the CRSS ratio among slip systems induces strain concentration [13].

The CRSS ratio in α-Ti changes with strain rates as well as the chemical composition and processing history. In α-Ti, the strain rate sensitivity of CRSS for Pri < a > is greater than that of the Bsl < a > [16,17]. Okamoto et al. conducted a crystal plasticity analysis to study the uniaxial deformation of polycrystalline α-Ti with an RD-split texture, considering the differences in strain rate sensitivities among slip systems [18]. With increases in strain rates, Pri < a > activity can decrease in the most of volumes in the specimen while non-Pri < a >, such as Bsl < a > and Pyr < a > increase locally. However, the above study focused on the strain redistribution mechanism occurring in the RD-split texture, and the activities of individual slip systems in other textures remain unknown. However, the activities of slip systems depending on microstructures can be

quantitatively evaluated by crystal plasticity analysis [6,8,13,14,19,20]. Further, this method can also be used to evaluate the dependence of slip system activities depending on the textures and strain rates in polycrystalline α-Ti [13]. Notably, crystal plasticity analysis with a rate-dependent single crystal constitutive equation reasonably predicts strain-rate dependent polycrystalline behavior based on the experimentally reported strain rate sensitivity of single crystal alpha-Ti [16,17]. Regardless of the capability of the prediction, systematic study of strain rate sensitivity of textured poly-crystalline alpha-Ti has not been performed so far. This study focuses on the investigation of activity of slip systems in polycrystalline level.

Crystallographic textures typically observed in α-Ti are shown in Table 1, and change with chemical composition and processing history [21]. As stated above, systematic investigation of slip system activities in individual textures has not been investigated in α-Ti. In this study, we investigated the activities of individual slip systems in polycrystalline α-Ti depending on strain rates and textures using crystal plasticity analysis. This paper is organized as follows. First, we explain the geometric model and crystal orientations for crystal plasticity analysis. We prepared three types of textures for the analysis: (i) RD-split texture, (ii) TD-split texture in which aggregates of (0001) axis divide in the TD, and (iii) basal texture in which the (0001) axes align in the direction

normal to the RD and TD (ND). Further, small and large scatterings of crystal orientations were specified in each texture model. Second, we explain the method for the crystal plasticity analysis employed in this study and the conditions for the analysis. Third, the activities for individual slip systems depending on textures and strain rates are demonstrated, and finally, we infer the conditions for crack initiation from the results of local slip activation, which occur easily.

2. Geometric models for crystal plasticity analysis

2.1 Microstructure reproduction

The geometric model representing the microstructure of polycrystalline α-Ti employed in this study is shown in Fig. 1. Voronoi tessellation, which was used to reproduce microstructures in polycrystalline materials [22][23][24][25], was employed to build the model. A brief description of Voronoi tessellation employed in this study is as follows: First, the material for the analysis is assumed. The points for crystal nucleation, where the number corresponds to crystal nuclei, are distributed within the material. Second, all the volumes divided in the material are assumed to belong to individual nearest nuclei, and then the regions consisting of divided volumes are classified by the

nuclei, where each classed region is assumed to be a crystal grain. The microstructures built by this method correspond to those obtained under the condition that crystal nuclei are generated simultaneously and grow isotropically. In this study, the size of the material is 800.0 μm × 600.0 μm × 8.0 μm and is divided into 100 × 75 × 1 voxels. Five hundred nuclei are randomly generated and grown isotropically within the material, and the microstructure obtained under this condition is shown in Fig. 1. Increasing the number of elements yields strain distributions with high resolution. However, if loss of information on crystallographic orientation distributions is little, the strain distributions are not strongly affected by the number of elements in crystal plasticity analysis [26]. Furthermore, in this study, we focus the current study on deformation behavior at the polycrystalline level and consider the computational cost, which resulted in the above number of elements adopted in the current analysis.

2.2 Textures

Crystal orientations are specified in individual grains of the geometric model shown in Fig. 1. Six texture models were built as shown in Fig. 2. Typical textures observed in α and near α-Ti are listed in Table 1 [21]. In this study, the axis orientations for RD-split, TD-split, and basal textures were selected from Table 1. (0001) axes of basal,

T, and R textures are aligned in a particular direction, and their crystal orientation distributions are the same with each other when their coordinate systems are rotated. Thus, the basal texture is selected to represent basal, T, and R textures. Small and large scatterings of crystal orientations are provided for the above three types of textures. Crystal orientations are expressed by a set of Euler angles (φ_1, Φ, φ_2) defined by Bunge, where φ_1 determines the rotation angle around (0001) axes and the direction of inclination of (0001) axes, Φ determines the inclination angle of (0001) axes, and φ_2 determines the rotation angle around (0001) axes. φ_1, Φ, and φ_2 are assigned according to the orientations described in Table 1. φ_2 is assigned by random numbers from 0° to 360°, and we employed the following values: (φ_1, Φ, φ_2) = (90°, ±20°, 0 to 360°) in RD-split texture, (0°, ±30°, 0° to 360°) in TD-split texture, and (φ_1, Φ, φ_2) = (0°, 0°, 0° to 360°) in basal texture, and the scattering of the (0001) axes in each texture is given by normal random numbers. The standard deviations for the random numbers were 10° and 40°. Models with small scatterings are defined as SD10, while those with large scatterings are defined as SD40. The pole figures for the textures obtained by the above conditions are shown in Fig. 2, and Fig. 3 shows the distributions of Schmid factors for < a > slip systems for the tensile direction, which are considered major active slip systems.

3. Methods for crystal plasticity analysis

In this study, a CPFE method incorporating the framework developed by Peirce et al. [27][28] was employed for deformation analysis. A brief description of the method is as follows. The activation of slip systems is assumed to follow the Schmid law, and the strain rate for each slip system is given by

$$\dot{\gamma}^{(i)} = \dot{\gamma}_0 sign\left(\tau^{(i)}\right)\left|\frac{\tau^{(i)}}{g^{(i)}}\right|^{1/m^{(i)}}, \tag{1}$$

where i, $\dot{\gamma}$, $\dot{\gamma}_0$, and τ correspond to the number of slip systems, shear slip rate, reference shear strain rate, and resolved shear stress (RSS), respectively. m is the slip rate sensitivity parameter; the CRSS changes more easily with the strain rate when m is large. In this study, the differences in the strain rate sensitivities of CRSS for individual slip systems are represented by different m values among slip systems. The value of g for Eq. (1) is obtained from Voce-type hardening law [29][30]:

$$\dot{g}^{(i)} = \frac{d\hat{\tau}}{d\Gamma}\sum_j h_{ij}\dot{\gamma}^{(i)}, \tag{2}$$

$$\hat{\tau}^{(i)} = \tau_0^{(i)} + \left(\tau_1^{(i)} + \theta_1^{(i)}\Gamma\right)\left\{1 - \exp\left(-\frac{\theta_0^{(i)}\Gamma}{\tau_1^{(i)}}\right)\right\}, \quad (3)$$

where Γ is the cumulative slip strain considering all slip systems and h_{ij} is the hardening matrix. τ_0, τ_1, θ_0, and θ_1 are the parameters to represent the relationships between shear stress and shear strain.

4. Conditions for crystal plasticity analysis

The elastic constants of pure titanium [31], shown in Table 2, were employed for CPFE analysis. The work hardening parameters are shown in Table 3, and the relationship between $\hat{\tau}$ and Γ is shown in Fig. 4a, where $\hat{\tau}$ determines the CRSS for each slip system. CRSSs in α-Ti vary not only with the chemical composition [28] but also with the processing history and conditions. Thus, the CRSS ratio may differ between α-Ti alloys even when their chemical compositions are the same [33]. In this study, CRSS values were determined as described by Warwick et al. [34] and Kawano et al. [13]. Twinning is assumed to be inactive as titanium alloys contain a substantial amount of O or >7.0% Al [2][35][36]. While it is possible that work softening occurs in <a> slip systems depending on the conditions in α-Ti [37][38], this study ignores the softening. Further, we assume that the work hardening is negligible in < a > slip systems and occurs slightly in < c + a > slip systems, as shown in Fig. 4a.

The values of *m*, which determine the strain rate sensitivities of CRSS, are listed in Table 4. The *m* values for Bsl <a> and Pri < a > are determined based on the experimental results obtained by Jun et al. [16] and Chatterjee et al. [17], and *m* for Pri < a > is larger than that for Bsl < a >. The *m* value of 0.02 was used for other slip systems employed in CPFE analysis [14][33]. Thus, the *m* values for Pyr < a > and < c + a > slip systems were not obtained experimentally. However, the activity for < c + a > slip systems is low owing to the high CRSS, and the change in CRSS with strain rate is limited in the activity of < c + a > slip systems. In contrast, previous reports [39][40] indicate that CRSS for Pyr < a > may be relatively low, and it is possible that its activation influences the activity of other slip systems [13]. As stated above, the precise CRSS of Pyr < a > depending on the strain rate is unknown. Thus, two conditions for Pyr < a > are employed in this study; the first condition is that only Bsl < a > and Pri < a > are activated (BP condition), and the second is that all slip systems are activated (AS condition). Under AS condition, while < c + a > slip systems are activated, the activity is quite low because of high CRSS, and the activation of < c + a > slip systems has a negligible impact on the activity of other slip systems.

Fig. 4b shows the initial CRSSs for Bsl < a > and Pri < a > in a single α-Ti as a function of the strain rates obtained by CPFE analysis [18]. The CRSSs for both slip

systems increase with increasing strain rates; however, the sensitivity of strain rates is different between them, and the CRSSs are similar when the strain rate is high.

The boundary conditions employed for the CPFE analysis are shown in Fig. 1, where the left-hand side plane perpendicular to the X-direction was fixed in the X-direction, and a forced displacement in the X-direction was applied to the right-hand side plane perpendicular to the X-direction. Two strain rate conditions were employed: (i) 1.0×10^{-4} s^{-1} (low strain rate condition) and (ii) 1.0×10^{-1} s^{-1} (high strain rate condition). The zero-stress condition is applied to other planes, except for those perpendicular to the X-direction.

5. Results and discussions

5.1 Macroscopic stress–strain relationship

Before investigating the microscopic strain concentration mechanisms, we investigated the macroscopic stress–strain relationship depending on the textures and strain rates. Fig. 5 shows the relationship between the nominal strain and stress. The yield points increased with strain rates under all conditions. This reflects the increases of initial CRSS with increasing strain rates as shown in Fig. 4b. This increase in yield points with

strain rates was also observed experimentally [41] while the strain rate dependency obtained in the current analyses was stronger than that in the experiment. These stress–strain relationships depending on strain rates were similar among the textures analyzed for the current simulation conditions.

The effects of scattering of crystal orientation on the macroscopic stress–strain relationship are small; however, the difference in flow stress between SD10 and SD40 is larger in the RD-split texture than those in the TD-split and basal textures. This slight difference among textures is derived from the activity of slip systems due to the difference in Schmid factors between textures as shown in Fig. 3. Typically, the activation of Pri < a > would have larger effects on the macroscopic stress-strain relationships. We quantitatively demonstrate the activity of each slip system in the next section.

5.2 Activity of slip systems depending on textures and strain rates

In this section, we investigate the activity of slip systems depending on the textures and strain rates. The activity of the slip systems is investigated using the distributions of slip strains in two-dimensional planes, followed by a more quantitative investigation using the line profiles of slip strains. High strain was observed both within and inner the grains. This will be related to the crystallographic orientation relationship

between grains [4][5]. However, in this study, we focus on the strain distribution at the polycrystalline level and will systematically investigate the intragranular inhomogeneity in the future works.

Fig. 6 shows the distributions of slip strain for the < a > slip systems under the SD10 condition. The activities of the < c + a > slip systems are relatively low, and the distributions are not shown. In the RD-split texture with the AS condition (Fig. 6a RD-split texture), Pri < a > activity decreases with strain rates while the Pyr < a > activity increases with the strain rates. Conversely, in RD-split texture with BP condition (Fig. 6b RD-split texture), the activity of Bsl < a > increases with strain rates while the activity of Pri < a > decreases with strain rates. This difference in activities is because the strain rate sensitivity of CRSS for Pri < a > is higher than those for other slip systems, and the deformation volume by activation of Pri <a> decreases with high strain rates. Thus, when activity of Pri <a> decreases with strain rates, other slip systems are required to be activated to supply the shortage of deformation volume arising from the decreasing activity of Pri < a >. The strain rate sensitivity of CRSS for Pyr < a > employed in this study has an unclear physical basis, and its accuracy is unknown. However, deformation analysis was performed under active and inactive conditions of Pyr < a >, and the results indicate the following. The activity of Pri < a > decreases with strain rates, while the

activity of non-Pri < a > increases with strain rates in the RD-split texture. In non-Pri < a > activation, Bsl <a> activity can be suppressed by Pyr < a > activation. A similar tendency was observed by Okamoto et al. [18].

In contrast, under the conditions of TD-split and basal textures (Fig. 6), the activity of Pri < a > is dominant. This variation is observed because the high Schmid factors for Pri < a > in TD and basal textures with SD10 conditions (Fig. 3a) strongly affect the activation of Pri < a > than large CRSS due to the strain rates. Therefore, while the difference in strain rate sensitivities of CRSSs among slip systems may induce changes in the activity of slip systems with strain rates, the tendency of the phenomena is different depending on the textures.

5.3 Effects of variety of crystal orientations

The scattering of crystal orientations occurs in actual textures, and the effects of scattering on the activities of slip systems are investigated in this section. Fig. 7 shows the distributions of slip strains when large scattering occurs in crystal orientations (i.e., the results obtained under SD40 condition). Activities of non-Pri < a > are higher under SD40 condition (Fig. 7) than those under SD10 (Fig. 6). The activities of the slip systems

in the individual textures are presented below.

In RD-split texture, while the strain rate sensitivities of slip system activities were similar between SD10 (Fig. 6) and SD40 (Fig. 7), slight variations in the distributions of slip strains were observed. Specifically, the activities of Bsl < a > and Pyr < a > are greater in SD40 than those in SD10. Typically, Bsl < a > was activated (Fig. 7) in TD-split and basal textures with SD40, which was not observed in SD10 (Fig. 6), and the activities of the system were higher at higher strain rates. This is because when large scattering occurs in crystal orientations, non-Pri < a > are activated in TD-split, basal, and RD-split textures and the activities of non-Pri < a > are higher with higher strain rates due to the strain rate sensitivities of CRSSs.

5.4 Local slip and its relaxation by activation of Pyr < a > slip systems

A quantitative evaluation of the activities in slip systems is conducted using line profiles. Fig. 8 shows the line profiles of slip strain, where only the results with high activity of non-Pri < a > are shown: the results of RD-split texture with SD10 and SD40, and those of basal texture with SD40. The local activation of slip systems was observed under the conditions shown in Fig. 8. Typically, strain concentration occurs more easily

in basal texture, which is caused by the scattering of aggregates of the (0001) axes. The inclination of the (0001) axis in the basal texture increases the Schmid factor for Bsl < a >, and grains with a high Schmid factor are distributed within the specimen when the scattering of (0001) axes are applied for grains. Strain tends to concentrate around such scattered regions with high Schmid factor, which easily undergo plastic deformation due to the strain redistribution mechanism between soft and hard regions [8][18]. In contrast, volume with high Schmid factor for Bsl < a > in RD-split texture is larger than that for basal texture as shown in Fig. 3, and the strain concentration of Bsl < a > is moderate in RD-split texture, compared to basal texture (Fig. 8). Furthermore, this ease of strain concentration has a strain rate dependency. Under all conditions in Fig. 8, slip strains of Pri < a > decreased and that of Bsl < a > or Pyr < a > increased with an increase in strain rates. That is, strain rates enhanced strain redistribution, and activities of non-Pri < a > increases locally by reducing activities in Pri < a > with an increase of strain rates. However, it is noted that strain rate sensitivity of CRSS for Pyr < a > is unclear, and Pri < a > may activate with high strain rate when the strain rate sensitivity of CRSS for Pyr < a > is higher than that of Pri < a >.

Next, the strain redistribution of non-Pri < a > with the strain rates is discussed. Under AS condition (Fig. 8a), the activity of Pyr < a > increases with strain rates, while

1 that of Pri < a > decreases. Then, the change in that of Bsl <a> with strain rates is relatively
2 slight. In contrast, under PB condition (Fig. 8b), while Pri < a > activity decreases, the
3 peaks of slip strain for Bsl < a > increases with strain rates, indicated by arrows in Fig.
4 8b. That is, activation of Bsl < a > is suppressed by that of Pyr < a >, and the same
5 tendency was observed in Okamoto et al. [18].

6 Finally, we discuss the relationship between the above results and the crack
7 nucleation mechanism. Crack nucleation along slip planes for Bsl < a >, Pri < a >, and
8 Pyr < a > were commonly observed [41]. In bimodal Ti-64, cracks were observed in the
9 planes along the slip planes for Bsl < a > and Pri < a > [42]. Thus, cracks are nucleated
10 along the planes in which the activities of the slip systems are high. While twinning plays
11 an important role in crack nucleation in pure titanium and commercially pure titanium
12 under cyclic loading [43], the addition of a large amount of O or Al (above 7%) suppresses
13 twinning [2][35] [36]. O and Al increase the c/a ratio [36] [39][44][45], and differences
14 in the CRSS between Pri < a > and non-Pri < a > decreases by the addition of such alloying
15 elements. In this study, the CRSS for Pri < a > is close to that of Bsl < a >. Therefore, the
16 results of this study would represent deformation mechanism in α-Ti with a high c/a ratio.
17 In such α-Ti with an RD-split or basal texture, non-Pri < a > may activate locally under
18 RD tensile deformation, and the activity increases with strain rates. Under these

conditions, it is predicted that crack nucleation is induced by non-Pri < a > activation and scattering of crystal orientations in textures.

Importantly, the numerical results in this study should be experimentally confirmed in the further study. In the experiment, texture, chemical composition and oxide concentration, which could affect activities and strain rate sensitivity of each deformation modes, must be carefully selected.

6. Conclusions

In this study, we conducted CPFE analysis of uniaxial tensile deformation in polycrystalline α-Ti with RD-split, TD-split, and basal textures. Small and large scatterings of crystal orientations are provided in individual textures; models with small and large scatterings are called SD10 and SD40, respectively. Differences in the strain rate sensitivities for CRSSs for individual slip systems were incorporated in all analyses. We investigated the relationship between the local activation of slip systems and effects of textures and CRSS depending on strain rates. The results can be summarized as follows:

1. The increase in macroscopic flow stress with strain rates was reproduced by CPFE

analysis. Scattering in crystal orientations has a negligible impact on the macroscopic stress–strain relationship for all textures.

2. Scattering of the (0001) axes affected the local activation of the slip systems. Typically, basal slip systems activity is locally high in basal texture when large scattering occurs.
3. The activity of Pri <a> decreased with increasing strain rates. In contrast, non-Pri < a > is activated with increasing strain rates. While strain rate sensitivity of CRSS for Pyr < a > slip systems is unknown, the activity of Bsl < a >increases with strain rates on the condition that Pyr < a > activity is high, and decreases with strain rates on the condition that Pyr < a > activity is low. Thus, Activation of Pyr < a > suppresses that of Bsl <a>. However, the exchange of activities between slip systems does not occur depending on the textures and CRSS ratios owing to the low CRSSs and high Schmid factors for Pri <a>.

Acknowledgment

This study was supported by the ISIJ Research Promotion Grant “Establishment of the principle to design microstructure of ductile two-phase Ti alloys having strong resistance for fracture” and JSPS KAKENHI (grant number JP19K04983).

Data availability

The raw/processed data required to reproduce these findings cannot be shared at this time as the data also forms part of an ongoing study.

References

[1] M. Peters, J. Kumpfert, C.H. Ward, C. Leyens, Titanium alloys for aerospace applications, Adv. Eng. Mater. 5 (2003) 419–427. https://doi.org/10.1002/adem.200310095.

[2] G. Lütjering, J.C. Williams, Titanium, 2nd Edition (Engineering and Processes), Springer Berlin Heidelberg, Berlin, Heidelberg, 2007. https://doi.org/10.1007/978-3-540-73036-1.

[3] M.R. Bache, A review of dwell sensitive fatigue in titanium alloys: the role of microstructure, texture and operating conditions, Int. J. Fatigue. 25 (2003) 1079–1087. https://doi.org/10.1016/S0142-1123(03)00145-2.

[4] F.P.E. Dunne, A. Walker, D. Rugg, A systematic study of hcp crystal orientation and morphology effects in polycrystal deformation and fatigue, Proc. R. Soc. A

Math. Phys. Eng. Sci. 463 (2007) 1467–1489.
https://doi.org/10.1098/rspa.2007.1833.

[5] F.P.E. Dunne, D. Rugg, A. Walker, Lengthscale-dependent, elastically anisotropic, physically-based hcp crystal plasticity: Application to cold-dwell fatigue in Ti alloys, Int. J. Plast. 23 (2007) 1061–1083. https://doi.org/10.1016/j.ijplas.2006.10.013.

[6] D. Raabe, M. Sachtleber, Z. Zhao, F. Roters, S. Zaefferer, Micromechanical and macromechanical effects in grain scale polycrystal plasticity experimentation and simulation, Acta Mater. 49 (2001) 3433–3441. https://doi.org/10.1016/S1359-6454(01)00242-7.

[7] Z. Zhao, M. Ramesh, D. Raabe, A.M. Cuitiño, R. Radovitzky, Investigation of three-dimensional aspects of grain-scale plastic surface deformation of an aluminum oligocrystal, Int. J. Plast. 24 (2008) 2278–2297. https://doi.org/10.1016/j.ijplas.2008.01.002.

[8] C.R. Weinberger, C.C. Battaile, H. Lim, J.D. Carroll, B.L. Boyce, T.E. Buchheit, Grain-scale experimental validation of crystal plasticity finite element simulations of tantalum oligocrystals, Int. J. Plast. 60 (2014) 1–18. https://doi.org/10.1016/j.ijplas.2014.05.004.

[9] C.C. Tasan, M. Diehl, D. Yan, C. Zambaldi, P. Shanthraj, F. Roters, D. Raabe, Integrated experimental-simulation analysis of stress and strain partitioning in multiphase alloys, Acta Mater. 81 (2014) 386–400. https://doi.org/10.1016/j.actamat.2014.07.071.

[10] A. Guery, F. Hild, F. Latourte, S. Roux, Slip activities in polycrystals determined by coupling DIC measurements with crystal plasticity calculations, Int. J. Plast. 81 (2016) 249–266. https://doi.org/10.1016/j.ijplas.2016.01.008.

[11] Z. Zhang, D. Lunt, H. Abdolvand, A.J. Wilkinson, M. Preuss, F.P.E. Dunne, Quantitative investigation of micro slip and localization in polycrystalline materials under uniaxial tension, Int. J. Plast. 108 (2018) 88–106. https://doi.org/10.1016/j.ijplas.2018.04.014.

[12] Y. Kawano, T. Ohashi, T. Mayama, M. Mitsuhara, Y. Okuyama, M. Sato, Crystal Plasticity Analysis of Microscopic Deformation Mechanisms and GN Dislocation Accumulation Depending on Vanadium Content in β Phase of Two-Phase Ti Alloy, Mater. Trans. 60 (2019) 959–968. https://doi.org/10.2320/matertrans.M2019016.

[13] Y. Kawano, T. Ohashi, T. Mayama, M. Tanaka, Y. Okuyama, M. Sato, Investigation of strain redistribution mechanism in α titanium by image-based

crystal plasticity analysis, Eur. Phys. J. B. 92 (2019) 204. https://doi.org/10.1140/epjb/e2019-100238-3.

[14] P. Baudoin, T. Hama, H. Takuda, Influence of critical resolved shear stress ratios on the response of a commercially pure titanium oligocrystal: Crystal plasticity simulations and experiment, Int. J. Plast. 115 (2019) 111–131. https://doi.org/10.1016/j.ijplas.2018.11.013.

[15] Y. Kawano, T. Ohashi, T. Mayama, R. Kondou, Crystal plasticity analysis of change in incompatibility and activities of slip systems in α-phase of Ti alloy under cyclic loading, Int. J. Mech. Sci. 146–147 (2018) 475–485. https://doi.org/10.1016/j.ijmecsci.2017.09.023.

[16] Z. Zhang, T.S. Jun, T.B. Britton, F.P.E. Dunne, Intrinsic anisotropy of strain rate sensitivity in single crystal alpha titanium, Acta Mater. 118 (2016) 317–330. https://doi.org/10.1016/j.actamat.2016.07.044.

[17] K. Chatterjee, J.Y.P. Ko, J.T. Weiss, H.T. Philipp, J. Becker, P. Purohit, S.M. Gruner, A.J. Beaudoin, Study of residual stresses in Ti-7Al using theory and experiments, J. Mech. Phys. Solids. 109 (2017) 95–116. https://doi.org/10.1016/j.jmps.2017.08.008.

[18] T. Okamoto, Y. Kawano, T. Mayama, M. Mitsuhara, S. Yamasaki, M. Ssto,

Numerical Analysis of Strain Rate Dependency on Activities of Slip Systems in Polycrystalline α-Ti, J. Soc. Mater. Sci. Japan (In Japanese). 70 (2021) 393–399. https://doi.org/10.2472/jsms.70.393.

[19] A. Guery, F. Hild, F. Latourte, S. Roux, Identification of crystal plasticity parameters using DIC measurements and weighted FEMU, Mech. Mater. 100 (2016) 55–71. https://doi.org/10.1016/j.mechmat.2016.06.007.

[20] P. Baudoin, T. Hama, S. Uchida, H. Takuda, Crystal plasticity analysis of the deformation of a grade 2 CP-Ti oligocrystal, J. Phys. Conf. Ser. 1063 (2018) 012048. https://doi.org/10.1088/1742-6596/1063/1/012048.

[21] H. Inoue, Textures in titanium and titanium alloys (in Japanese), Metal. 69 (1999) 30–38.

[22] Y. Kawano, T. Ohashi, A mesoscopic numerical study of sea ice crystal growth and texture development, Cold Reg. Sci. Technol. 57 (2009) 39–48. https://doi.org/10.1016/j.coldregions.2009.02.001.

[23] Y. Kawano, T. Ohashi, Numerical study on c-axis orientations of sea ice surface grown under calm sea conditions using a particle method and Voronoi dynamics, Cold Reg. Sci. Technol. 112 (2015) 29–38. https://doi.org/10.1016/j.coldregions.2014.12.012.

[24] I. Simonovski, L. Cizelj, Automatic parallel generation of finite element meshes for complex spatial structures, Comput. Mater. Sci. 50 (2011) 1606–1618. https://doi.org/10.1016/j.commatsci.2010.12.014.

[25] F. Sun, E.D. Meade, N.P. O′Dowd, Microscale modelling of the deformation of a martensitic steel using the Voronoi tessellation method, J. Mech. Phys. Solids. 113 (2018) 35–55. https://doi.org/10.1016/j.jmps.2018.01.009.

[26] Y. Kawano, T. Ohashi, T. Mayama, M. Tanaka, M. Sakamoto, Y. Okuyama, M. Sato, Development of a EBSD-FEM data conversion interface and the image-based crystal plasticity analysis, Trans. JSME (in Japanese). 84 (2018) 17-00559:1–18. https://doi.org/10.1299/transjsme.17-00559.

[27] D. Peirce, R.J. Asaro, A. Needleman, Material rate dependence and localized deformation in crystalline solids, Acta Metall. 31 (1983) 1951–1976. https://doi.org/10.1016/0001-6160(83)90014-7.

[28] R.J. Asaro, A. Needleman, Texture development and strain hardening in rate dependent polycrystals, Acta Metall. 33 (1985) 923–953. https://doi.org/10.1016/0001-6160(85)90188-9.

[29] E. Voce, A practical strain-hardening function, Metallurgia. 51 (1955) 219–226.

[30] U.F. Kocks, Laws for Work-Hardening and Low-Temperature Creep, J. Eng.

Mater. Technol. 98 (1976) 76–85. https://doi.org/10.1115/1.3443340.

[31] E.S. Fisher, C.J. Renken, Single-crystal elastic moduli and the hcp → bcc transformation in Ti, Zr, and Hf, Phys. Rev. 135 (1964). https://doi.org/10.1103/PhysRev.135.A482.

[32] J.C. Williams, R.G. Baggerly, N.E. Paton, Deformation behavior of HCP Ti-Al alloy single crystals, Metall. Mater. Trans. A. 33 (2002) 837–850. https://doi.org/10.1007/s11661-002-0153-y.

[33] T. Hama, A. Kobuki, H. Takuda, Crystal-plasticity finite-element analysis of anisotropic deformation behavior in a commercially pure titanium Grade 1 sheet, Int. J. Plast. 91 (2017) 77–108. https://doi.org/10.1016/j.ijplas.2016.12.005.

[34] J.L.W. Warwick, N.G. Jones, K.M. Rahman, D. Dye, Lattice strain evolution during tensile and compressive loading of CP Ti, Acta Mater. 60 (2012) 6720–6731. https://doi.org/10.1016/j.actamat.2012.08.042.

[35] S. Hanada, Plastic Deformation Mechanisms in α Titanium, Tetsu-to-Hagane (in Japanese). 76 (1990) 495–502. https://doi.org/10.2355/tetsutohagane1955.76.4_495.

[36] A. Fitzner, D.G.L. Prakash, J.Q. Da Fonseca, M. Thomas, S.Y. Zhang, J. Kelleher, P. Manuel, M. Preuss, The effect of aluminium on twinning in binary

alpha-titanium, Acta Mater. 103 (2016) 341–351. https://doi.org/10.1016/j.actamat.2015.09.048.

[37] D.C. Pagan, P.A. Shade, N.R. Barton, J.-S. Park, P. Kenesei, D.B. Menasche, J. V. Bernier, Modeling slip system strength evolution in Ti-7Al informed by in-situ grain stress measurements, Acta Mater. 128 (2017) 406–417. https://doi.org/10.1016/j.actamat.2017.02.042.

[38] L. Wang, Z. Zheng, H. Phukan, P. Kenesei, J.S. Park, J. Lind, R.M. Suter, T.R. Bieler, Direct measurement of critical resolved shear stress of prismatic and basal slip in polycrystalline Ti using high energy X-ray diffraction microscopy, Acta Mater. 132 (2017) 598–610. https://doi.org/10.1016/j.actamat.2017.05.015.

[39] H. Conrad, Effect of interstitial solutes on the strength and ductility of titanium, Prog. Mater. Sci. 26 (1981) 123–403. https://doi.org/10.1016/0079-6425(81)90001-3.

[40] B. Barkia, V. Doquet, J.P. Couzinié, I. Guillot, E. Héripré, In situ monitoring of the deformation mechanisms in titanium with different oxygen contents, Mater. Sci. Eng. A. 636 (2015) 91–102. https://doi.org/10.1016/j.msea.2015.03.044.

[41] I. Bantounas, D. Dye, T.C. Lindley, The role of microtexture on the faceted fracture morphology in Ti–6Al–4V subjected to high-cycle fatigue, Acta Mater.

58 (2010) 3908–3918. https://doi.org/10.1016/j.actamat.2010.03.036.

[42] K. Le Biavant, S. Pommier, C. Prioul, Local texture and fatigue crack initiation in a Ti-6Al-4V titanium alloy, Fatigue <html_ent Glyph="@amp;" Ascii="&"/> Fract. Eng. Mater. Struct. 25 (2002) 527–545. https://doi.org/10.1046/j.1460-2695.2002.00480.x.

[43] N. Bosh, C. Müller, H. Mozaffari-Jovein, Deformation twinning in cp-Ti and its effect on fatigue cracking, Mater. Charact. 155 (2019). https://doi.org/10.1016/j.matchar.2019.109810.

[44] J.M. Oh, B.G. Lee, S.W. Cho, S.W. Lee, G.S. Choi, J.W. Lim, Oxygen effects on the mechanical properties and lattice strain of Ti and Ti-6Al-4V, Met. Mater. Int. 17 (2011) 733–736. https://doi.org/10.1007/s12540-011-1006-2.

[45] P. Kwasniak, M. Muzyk, H. Garbacz, K.J. Kurzydlowski, Influence of oxygen content on the mechanical properties of hexagonal Ti-First principles calculations, Mater. Sci. Eng. A. 590 (2014) 74–79. https://doi.org/10.1016/j.msea.2013.10.004.

Figure and table captions

Fig. 1 Polycrystalline model of α-Ti.

Fig. 2 Pole figures of (a) SD10 model and (b) SD40 model with RD-split, TD-split, and basal textures.

Fig. 3 Distributions of Schmid factors in (a) SD10 and (b) SD40 models.

Fig. 4 (a) $\hat{\tau}$ for each slip system as a function of cumulative slip strain and (b) initial CRSSs for Bsl < a > and Pri < a > depending on the strain rates [18].

Fig. 5 Profiles showing the relationship between nominal stress and strain obtained by models with RD-split texture (a, d), TD-split texture (b, e), and basal texture (c, f). Activation of Pyr < a > is considered in (a–c) and not considered in (d–f).

Fig. 6 Slip strain distributions when SD10 models are employed, and nominal strain is 2.0 %; (a) AS condition and (b) BP condition.

Fig. 7 Slip strain distributions when SD40 models are employed and nominal strain is 2.0 %; (a) AS condition and (b) BP condition.

Fig. 8 Line profiles of slip strain along X_1–X_2 in Fig. 1 when nominal strain is 2.0%; SD10 and SD40 models with RD-split texture and an SD40 model with basal texture with high strain rates on slip strains; (a) AS condition and (b) BP condition.

Table 1 Texture types and the orientation of their (0001) axis

Table 2 Elastic compliance of pure titanium [$(TPa)^{-1}$] [31]

Table 3 Values used for the Voce equation [MPa]

Table 4 Conditions of strain rate sensitivity *m* [16,17]

Figures

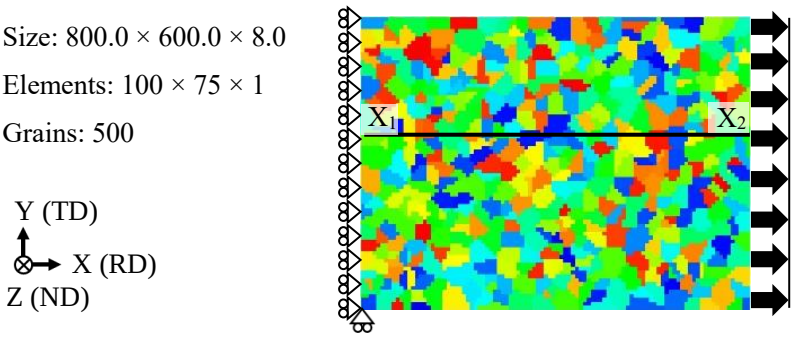

Fig. 1 Polycrystalline model of α-Ti.

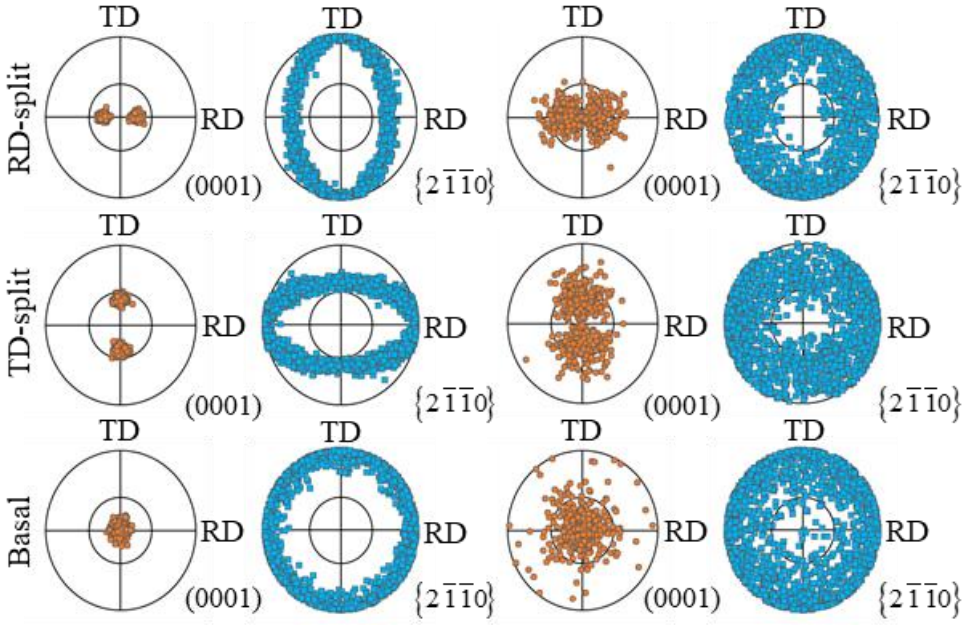

Fig. 2 Pole figures of (a) SD10 model and (b) SD40 model with RD-split, TD-split, and basal textures.

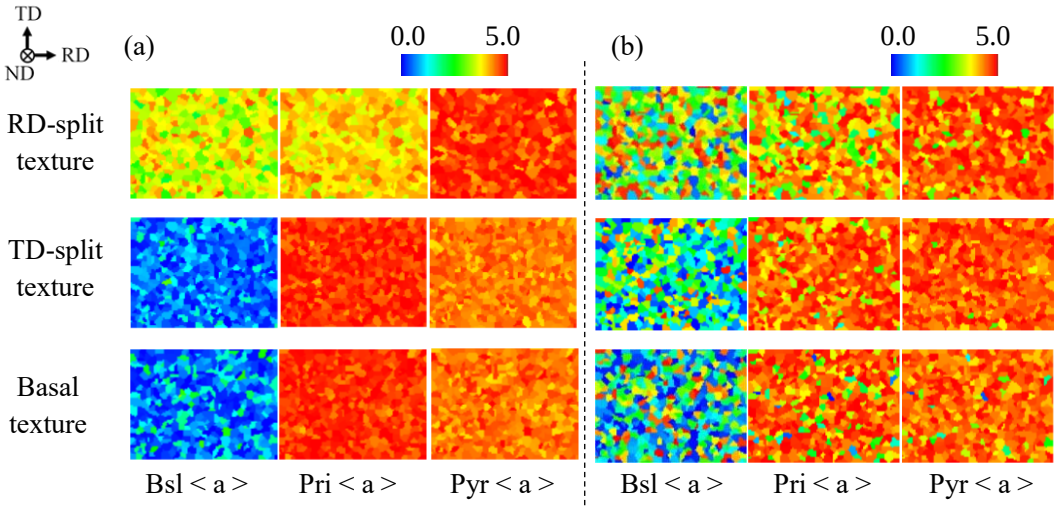

Fig. 3 Distributions of Schmid factors in (a) SD10 and (b) SD40 models.

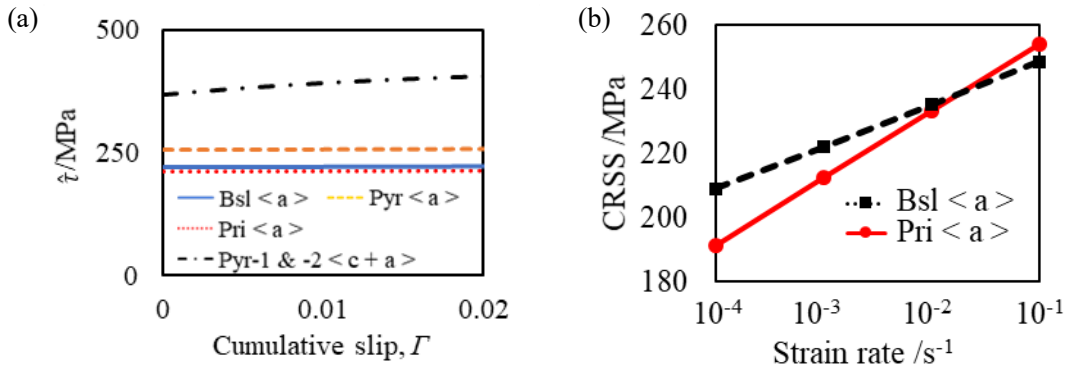

Fig. 4 (a) $\hat{\tau}$ for each slip system as a function of cumulative slip strain and (b) initial CRSSs for Bsl < a > and Pri < a > depending on the strain rates [18].

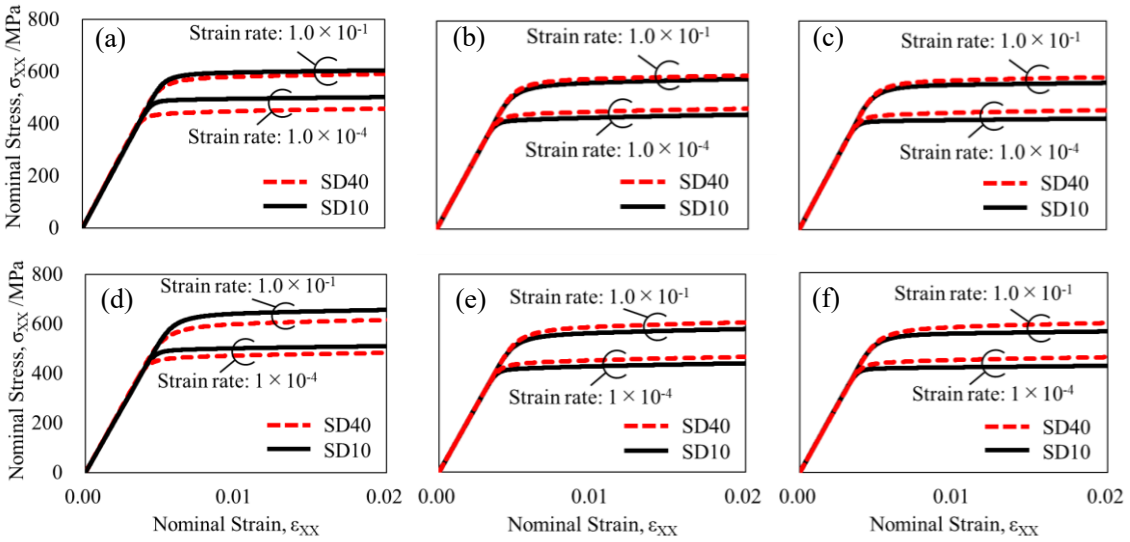

Fig. 5 Profiles showing the relationship between nominal stress and strain obtained by models with RD-split texture (a, d), TD-split texture (b, e), and basal texture (c, f). Activation of Pyr < a > is considered in (a–c) and not considered in (d–f).

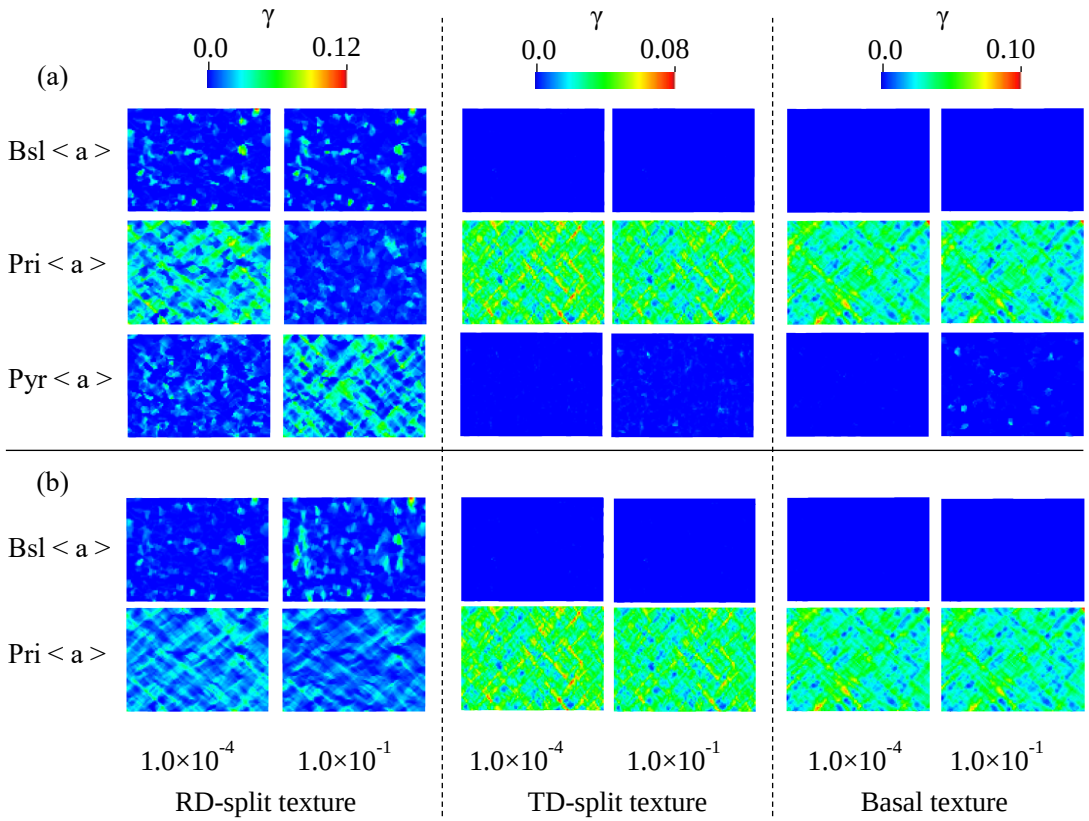

Fig. 6 Slip strain distributions when SD10 models are employed, and nominal strain is 2.0 %; (a) AS condition and (b) BP condition.

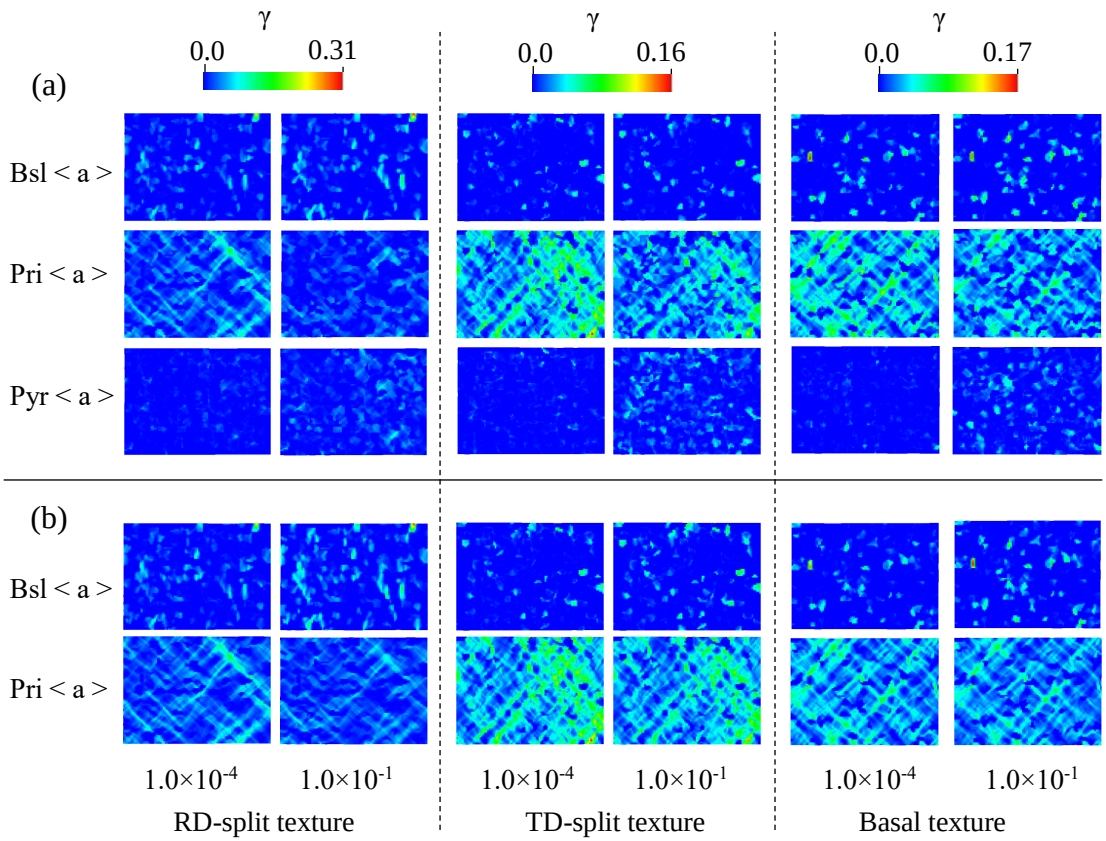

Fig. 7 Slip strain distributions when SD40 models are employed and nominal strain is 2.0 %; (a) AS condition and (b) BP condition.

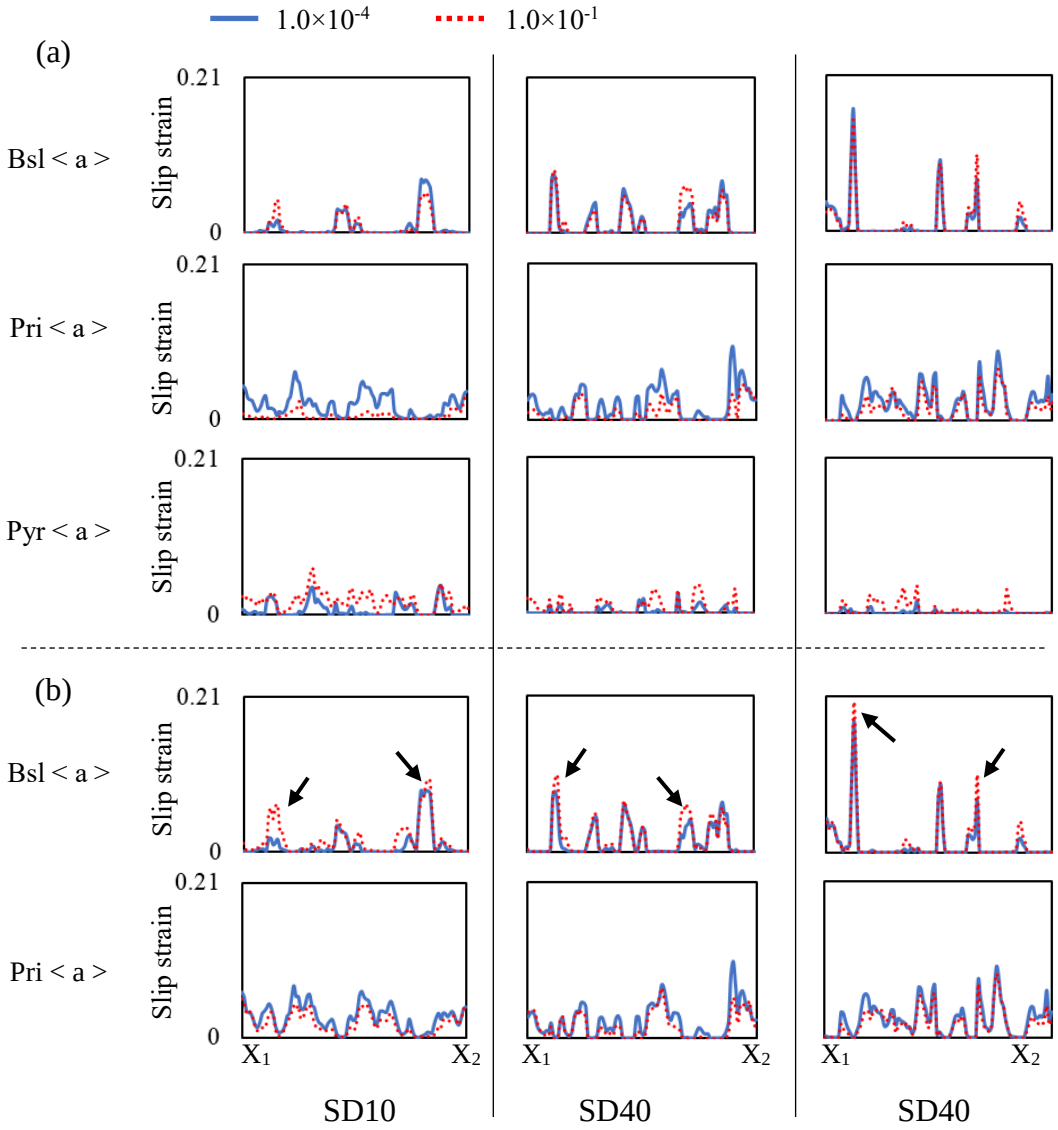

Fig. 8 Line profiles of slip strain along X_1–X_2 in Fig. 1 when nominal strain is 2.0%; SD10 and SD40 models with RD-split texture and an SD40 model with basal texture with high strain rates on slip strains; (a) AS condition and (b) BP condition.

1 Tables

2 Table 1 Texture types and the orientation of their (0001) axis

Texture types	Orientation of (0001) axis
RD-split	20°–30° inclination from ND to RD
TD-split	30°–40° inclination from ND to TD
Basal	Parallel to ND
T (Transverse)	Parallel to TD
R (RD)	Parallel to RD

3

4 Table 2 Elastic compliance of pure titanium [$(TPa)^{-1}$] [31]

S_{11}	S_{12}	S_{13}	S_{33}	S_{44}
9.581	-4.623	-1.893	6.983	21.413

5

6 Table 3 Values used for the Voce equation [MPa]

Slip systems		τ_0	τ_1	θ_0	θ_1
Bsl < a >		220	400	100	200
Pri < a >		210	400	100	200
Pyr-1 < a >	AS condition	255	400	100	200
	PB condition	Inactive			
Pyr-1 < c + a > and Pyr-2 < c + a >	AS condition	369	50	3000	100
	PB condition	Inactive			

7

8 Table 4 Table 4 Conditions of strain rate sensitivity *m* [16,17]

Bsl < a >	Pri < a >	Pyr-1 < a >	Pyr-1 < c + a > and Pyr-2 < c + a >
0.025	0.041	0.020	0.020

1